

# Core Precession and Global Modes in Granular Bulk Flow

Denis Fenistein, Jan-Willem van de Meent, and Martin van Hecke  
 Kamerlingh Onnes Lab, Leiden University, PObox 9504, 2300 RA Leiden, Netherlands  
 (Dated: January 24, 2022)

A transition from local to global shear zones is reported for granular flows in a modified Couette cell. The experimental geometry is a slowly rotating drum which has a stationary disc of radius  $R_s$  fixed at its bottom. Granular material, which fills this cell up to height  $H$ , forms a wide shear zone which emanates from the discontinuity at the stationary discs edge. For shallow layers ( $H/R_s \lesssim 0.55$ ), the shear zone reaches the free surface, with the core of the material resting on the disc and remaining stationary. In contrast, for deep layers ( $H/R_s \gtrsim 0.55$ ), the shear zones meet below the surface and the core starts to precess. A change in the symmetry of the surface velocities reveals that this behavior is associated with a transition from a local to a global shear mode.

PACS numbers: 45.70.Mg, 45.70.-n, 83.50.Ax, 83.85.Cg

Slowly sheared granular matter usually organizes into rigid regions separated by narrow shear bands where the material yields and flows [1, 2, 3, 4, 5, 6, 7, 8]. Such grain flows appear to prohibit successful continuum modeling – not only because of the steep gradients in velocity, but also because subtle microscopic characteristics of the granulate can alter the flow in a qualitative manner [6].

The formation of narrow shear bands can be avoided by driving the granulate from a discontinuity in the bottom support of the grain layer (Fig. 1a), effectively pinning a wide shear zone away from the sidewalls [9]. The resulting grain flows are smooth and robust, with both velocity profiles and shear zone location exhibiting simple, grain independent properties – these flows should be amenable to a continuum description. At present, a simple model aimed at describing an infinitely narrow shear band captures the location of the shear zone [10], but there are no models which describe the finite width or velocity profile of the shear zones found in experiment. In this Letter we uncover a novel transition of the flow in this system which occurs for deep grain layers.

The flows of *shallow* layers of granular materials in our setup are characterized by wide shear zones. The surface velocities are azimuthal and proportional to the driving rate  $\Omega$ , and the ratio of the average angular surface velocity and  $\Omega$ , denoted  $\omega(r)$ , is well fitted by [9]:

$$\omega(r) = \text{nerf}\left(\frac{r - R_c}{W}\right), \quad (1)$$

where  $r$  is the radial coordinate,  $R_c$  and  $W$  parameterize the location and width of the shear zones, and  $\text{nerf}(x)$  denotes the normalized errorfunction  $1/2 + 1/2 \text{erf}(x)$ .  $W$  is independent of disc radius  $R_s$  and grows with grain diameter  $d$  and layer height  $H$  as [9]

$$W/d \sim (H/d)^{2/3} \leftrightarrow W \sim H^{2/3} d^{1/3}, \quad (2)$$

while  $R_c$  is independent of  $d$  [9]:

$$1 - R_c/R_s = (H/R_s)^{5/2}. \quad (3)$$

When  $H/R_s$  is small,  $\omega$  tends to zero for small  $r$  – the core material remains *stationary* in shallow layers. The

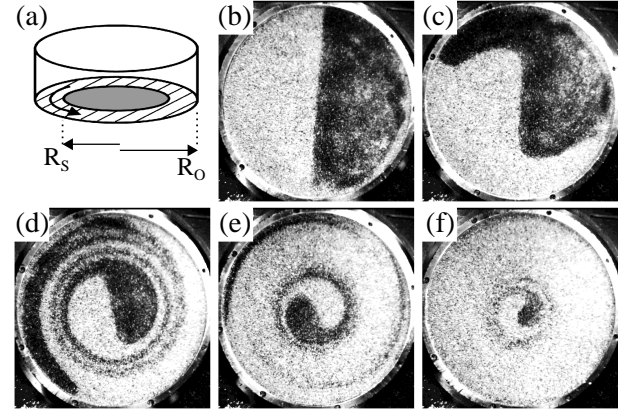


FIG. 1: (a) Schematic side-view of our split-bottomed shear cell, showing a stationary bottom disk of radius  $R_s$  (grey), the rotating bottom ring (striped) and rotating outer cylinder of radius  $R_o = 105$  mm. (b-f) Series of snapshots of top-views of our setup (for  $R_s = 95$  mm and  $H = 60$  mm), where colored particles sprinkled on the surface illustrate the core precession for  $t = 0$  s (b),  $t = 10$  s (c),  $t = 10^2$  s (d),  $t = 10^3$  s (e) and  $t = 10^4$  s (f).

inward shift of  $R_c$  with  $H/R_s$  (Eq. (3)) implies, however, that this behavior should break down eventually.

Figs. 1b-f illustrate novel flow patterns, characteristic for *deep* layers. The most striking feature is that the core starts to precess with a nonzero rate  $\omega_p = \omega(r \rightarrow 0)$ . Precession is not simply the consequence of the overlap of the two opposing shear zones given by Eq. (1) at  $r = \pm R_c$ , since before being eroded by shear, the inner core rotates as a solid blob for an appreciable time (Fig. 1(b-f)).

In this Letter we will characterize the transition to precession, and specifically address the following questions: How does  $\omega_p$  grow with layer depth? What are the velocity profiles for such deep layers? What happens to the scaling relations Eq. 2-3? What underlies this transition?

*Setup* – Our setup is a modified version of the disk geometry described in earlier work [9], and consists of a stationary bottom disk of radius  $R_s$ , a rotating bottom

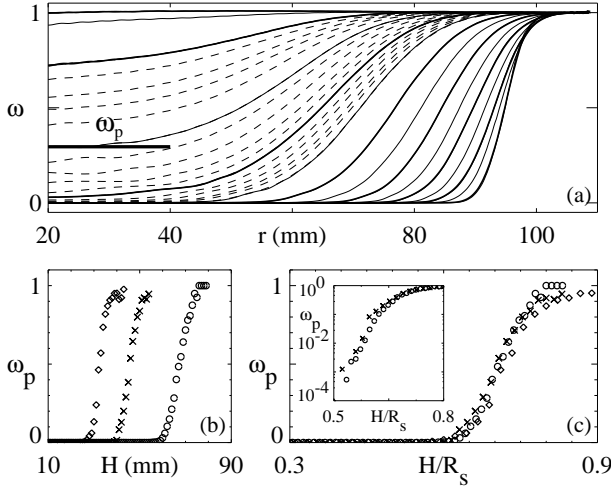


FIG. 2: (a) Surface velocity profiles  $\omega(r)$  for  $R_s = 95$  mm and increasing layer depth. Thick curves:  $H = 10, 20, \dots, 80$  mm; Thin curves  $H = 15, 25, \dots, 75$  mm; Dashed curves  $H = 56, 56, \dots, 69$  mm. Precession gradually sets in for  $H \gtrsim 60$  mm. The thick line indicates the nonzero plateau value  $\omega_p$  for  $H = 65$  mm. (b) Precession rate  $\omega_p$  as function of  $H$  for  $R_s = 45$  mm (diamonds),  $R_s = 65$  mm (x) and  $R_s = 95$  mm (circles). (c) Precession rate curves collapse when plotted as function of  $H/R_s$ . The inset shows that  $\omega_p$  grows smoothly with  $H/R_s$ .

ring and outer cylinder of radius  $R_o = 105$  mm (Fig. 1a). The disc radius  $R_s$  can be varied from 45 mm to 95 mm. The cell is filled to a height  $H$  with a polydisperse mixture of spherical glass beads with diameters ranging from 0.6 to 0.8 mm; a layer of grains is glued to the side walls and bottom rings to obtain rough boundaries. Slow flows are rate-independent, i.e., surface velocities are proportional to the rotation rate  $\Omega$  of outer cylinder and its co-moving ring. We fix  $\Omega$  at 0.15 rad/s, and recover the surface velocity by a variant of particle image velocimetry (for more details see [9]).

**Basic phenomenology** – Figs. 2-3 illustrate the main features of the surface velocity profiles  $\omega(r)$  as function of increasing layer depth  $H$ . For shallow layers ( $H/R_s \lesssim 0.5$ ) the data is well fitted by Eq. 1. The core precession, which sets in for  $H/R_s \lesssim 0.65$  constitutes the clearest deviation from this simple form. For  $H/R_s \gtrsim 0.8$   $\omega_p$  tends to one, and the whole surface rotates then rigidly. Apparently the shear zone remains confined below the surface in this case.

In Fig. 2b-c we show that the data for  $\omega_p$  collapses when plotted as function of  $H/R_s$ . The data suggests a much faster than exponential growth in the initial stages (i.e. when  $\omega_p \ll 1$ ) as illustrated in the inset of Fig. 2c). Before precession becomes appreciable, the left-right symmetry of  $\omega(r)$  is broken:  $\omega(\Delta r - R_c) \neq 1 - \omega(R_c - \Delta r)$ . As illustrated in Fig. 3, the right (large  $r$ ) tail of  $\omega(r)$  is then significantly steeper than its left (small  $r$ ) tail.

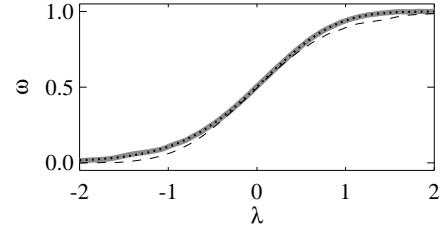


FIG. 3: Illustration of broken left-right symmetry of  $\omega$  for  $R_s = 95$  mm and  $H = 58$  mm, where  $\lambda$  denotes the rescaled spatial coordinate  $((r - R_c)/R_s)$ . Shown are  $\omega(\lambda)$  (grey), its symmetric counterpart  $1 - \omega(-\lambda)$  (dashed) and the best fit of  $\omega(\lambda)$  to Eq. (4) (dots).

Hence, three regimes can be distinguished. *Shallow layers* occur for  $H/R_s \lesssim 0.45$  where  $\omega_p$  is zero,  $\omega(r)$  is symmetric and Eq. 1 fits the data well. *Deep layers* occur for  $H \gtrsim 0.65$ , where the reflection symmetry of zones is strongly broken and precession sets in. In the *crossover regime*,  $0.45 \lesssim H \lesssim 0.65$ , the symmetry of  $\omega(r)$  is broken but  $\omega_p$  remains small.

**Transition from local to global modes** – Both symmetry breaking and precession reflect the same underlying change in the qualitative nature of the shear modes. Since  $\omega(r)$  in general can be written as  $\text{nerf}[\chi(r)]$ , we have calculated  $\chi(r) := \text{nerf}^{-1}[\omega(r)]$  from our experimentally obtained velocity profiles. The resulting  $\chi(r)$  are shown in Fig. 4a. For shallow layers  $\chi(r)$  is a linear function, consistent with the fact that  $\omega(r)$  obeys Eq. (1). For deep layers,  $\chi(r)$  becomes a nonlinear function and over the whole range of  $H$ ,  $\chi(r)$  can be fitted well by an empirical third order polynomial [11] (see Fig. 4a):

$$\chi(r) = a_0 + a_1 r + a_3 r^3. \quad (4)$$

**Both precession and symmetry breaking are well captured by this fit.** As shown in Fig. 4b-c, the three aforementioned regimes have now a simple interpretation in terms of the linear ( $a_1$ ) and cubic ( $a_3$ ) coefficient. For shallow layers the cubic term vanishes while for deep layers the linear term is absent; both are nonzero in the crossover regime.

Note that the fit parameters  $a_1$  and  $a_3$  have dimensions of inverse length and inverse length cubed, and are therefore expected to scale as  $W$  and  $W^3$ . Rewriting Eq. 2 as  $W/(R_s^{2/3}d^{1/3}) \sim (H/R_s)^{2/3}$ , it follows that  $a_1 R_s^{2/3}d^{1/3}$  and  $a_3 R_s^2 d$  should collapse when plotted as function of  $H/R_s$  – indeed this is the case [12] (Fig. 4c).

The functional form for  $\omega$  for deep layers is thus

$$\omega(r) \approx \text{nerf}(a_0 + a_3 r^3), \quad (5)$$

while for shallow layers Eq. (1) can be rewritten as

$$\omega(r) \approx \text{nerf}(a_0 + a_1 r). \quad (6)$$

These two limits have different symmetries. For shallow layers, two flow profiles obtained for two different

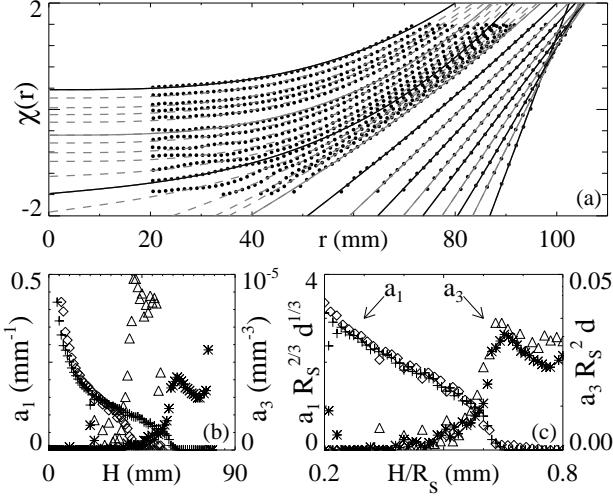


FIG. 4: (a) Profiles of  $\chi(r)$  for  $R_s = 95$  mm and increasing layer depth (dots), compared to cubic fits given by Eq. (4) (curves). Similar to Fig. 2a,  $H = 10, 15, 20, \dots, 55, 56, \dots, 70$  mm. (b) Fit parameters  $a_1$  for  $R_s = 65$  mm (diamonds) and 95 mm (+) and  $a_3$  for  $R_s = 65$  mm (triangles) and 95 mm (stars) as function of  $H$ . (c) Non-dimensionalized fit parameters as function of  $H/R_s$  (see text).

slip radii ( $R_{s1}$  and  $R_{s2}$ ) are simply related by translations of the radial coordinate via  $\omega(r - R_{s1})|_{R_{s1}, H} = \omega(r - R_{s2})|_{R_{s2}, H}$  – the shear zone is a *local* phenomenon, insensitive to the location of the center of the shear cell. For deep layers this symmetry is absent, and the shear mode is *global*. The precession and symmetry breaking of  $\omega(r)$  both reflect the crossover from a local to a global shear mode.

**3D flow structure** – In Fig. 5, the crucial difference between the 3D flow structure of shallow and deep layers is illustrated. The flow in the bulk has been probed by putting patterns of lines of colored tracer particles at given height in the bulk,  $H_b$ , adding more material so as to bury the line-pattern, rotating the system for a short period ( $\sim 8$  s), and recovering the deformed line-pattern by carefully removing the upper layers of grains [9]. The striking difference between these two cases where  $\omega_p \approx 0$  and a  $\omega_p \approx 0.8$  respectively, is that in the former case the shear zones reach the free surface while for the latter case the shear zones meet in the bulk. This scenario is consistent with the finding of recent MRI and numerical studies of the flow in this geometry [13, 14], and gives a straightforward interpretation of local and a global shear modes.

**Comparison to theory** – Recently, Unger *et al.* proposed a simple theory for the location of the shear zone in our system. They model the shear zone as an infinitely thin sheet along which the granulate slides, with the normal stress on the sheet given by hydrostatic pressure and the shear stress by sliding friction. By numerically adjusting the sheet so as to minimize the total torque, the

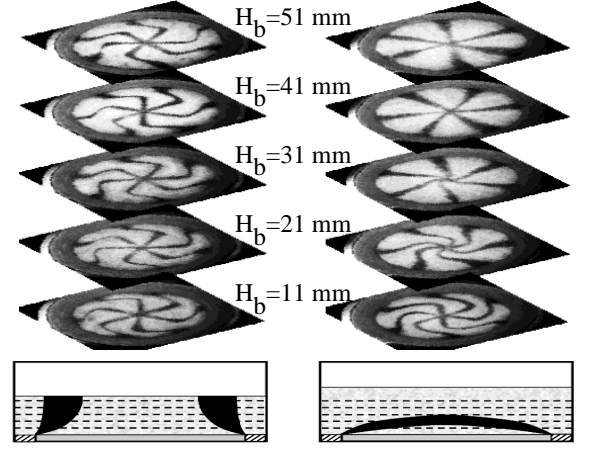


FIG. 5: 3D flow-profiles for  $R_s = 95$  mm. Both stacks show five slices at heights  $H_b = 11, 21, \dots, 51$  mm inside the material; the left stack is for layer depth  $H = 57$  mm, the right stack for  $H = 71$  mm. The bottom figures show sketches of the shear zones within the bulk (black) – the dashed curves indicate the heights  $H_b$  where the patterns were created.

theory predicts the shear zones location at the free surface,  $R_m(H)$ . This function is different from the simple scaling law Eq. (3), and the theory predicts that for deep layers the shear sheet no longer reaches the free surface but closes in the bulk; the two cases are separated by a first order (hysteretic) transition that occurs around  $H/R_s \approx 0.7$  [10]. While we have not found any evidence for hysteresis, the theory of Unger *et al.* does a good job in capturing the qualitative behavior.

To test the theory quantitatively, in Fig. 6 our data for the shear zones location is compared to  $R_m(H)$  and Eq. (3). For the general case, we have to define the center of general shear zones. There is no unique choice, and we have tested the following three expressions:

$$R_1 := \text{where } \omega(r) = 0.5, \quad (7)$$

$$R_2 := \text{where } \partial_r \omega(r) \text{ is maximal}, \quad (8)$$

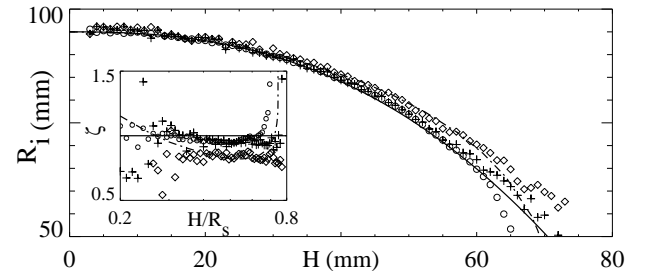


FIG. 6: Shear zone positions versus layer depth for  $R_s = 95$  mm, where circles, pluses and diamonds correspond to  $R_1$ ,  $R_2$  and  $R_3$  respectively, the solid curve is the scaling form given by Eq. (3) and the dashed curve is the result by Unger *et al.* [10]. The inset shows the same data, now in rescaled form, by defining  $\zeta := (1 - R_i/R_s)/(H/R_s)^{5/2}$ .

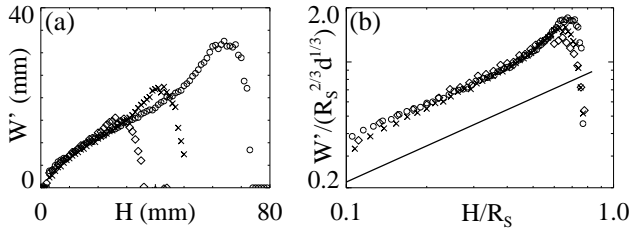


FIG. 7: (a) Shear zones width  $W'$  as function of  $H$  for  $R_s = 45, 65$  and  $95$  mm. For small heights the shearzone width is independent of  $R_s$ , while deviations start to set in for larger heights. (c) The nondimensionalized width  $W' R_s^{2/3} d^{1/3}$  follows a universal curve as function of  $H/R_s$ , which for small heights is approximated well by a powerlaw with exponent  $2/3$ , as indicated by the straight line.

$$R_3 := \text{where } \partial_r(r\omega(r)) \text{ is maximal.} \quad (9)$$

Note that for shear zones of the form Eq. (1),  $R_1$  and  $R_2$  coincide with  $R_c$ , while  $R_3$  corresponds to where the dimensional strain rate is maximal. As shown in Fig. 6, for shallow layers, both  $R_1$  and  $R_2$  are better described by Eq. (3) than by  $R_m$ , while  $R_3$  appears to be better described by  $R_m$ . For deep layers, the situation is more complicated, with neither model describing any of the three measured curves in detail.

*Open Questions* – There are three questions that we think deserve particular attention. The first concerns the functional form of  $\omega(r)$ . While it is now widely accepted that in many shear flows, the velocity profile across a shear band is smooth, it is not clear what mechanism selects this velocity profile, or indeed its “tail” [6]. In some systems, these tails appear exponential [15], for our shallow shear zones these tails are Gaussian [9], and our results here suggest that for deep layers, the tail stretching out into the material has a more complex form (Eq. (5)). Similarly, we do not know what determines the functional form or tails of  $\omega_p(H/R_s)$  (Fig. 2b-c). Theoretical work is very welcome here.

The second question concerns the finite width of the shear zones. Let us define the width  $W'$ , for general velocity profiles, as the interval where  $\omega$  grows from  $\omega_p + 0.1 \times (1 - \omega_p)$  to  $0.9 \times (1 - \omega_p)$  [16].  $W'$  does not depend on  $R_s$  for shallow layers, but  $R_s$  sets the scale where  $W'$  saturates; for deep layers, both the microscale ( $d$ ) and macroscale ( $R_s$ ) play a role (Fig. 7a). The ratio  $R_s/d$  between these scales can be conceived as the non-dimensionalized radius of curvature. Eq. (2), when rewritten as  $W'/d = (H/R_s)^{2/3} (R_s/d)^{2/3}$ , suggests to plot the rescaled width,  $W'/(R_s^{2/3} d^{1/3})$ , as function of  $H/R_s$  – as shown in (Fig. 7b), this leads to a good data-collapse. This result is consistent with the scaling with exponent  $2/3$  for shallow layers (Eq. (2)). It is not known what sets the value of this non-trivial exponent.

Finally, it is an open question whether the transition to precession should be conceived as a smooth crossover

or as a sharply defined transition. The smooth growth of  $\omega_p$  with  $H/R_s$  suggests a crossover (Fig. 2b-c), while the (critical) vanishing of  $a_1$  with  $(H/R_s)$  (Fig. 4b-c) suggests a sharp transition.

*Outlook* – A wide range of granular flows can be achieved in split bottom geometries. Detailed studies of the 3D structure of these flows [14], together with studies of the role of packing density [13], anisotropies [17] and contact forces [18] are uncovering the richness of slowly sheared granulates, and provide crucial ingredients for theories of flows of dense granular media. The robust behavior of grain flows in split bottom geometries hopefully will provide important testing ground for such theories [10, 19].

*Acknowledgments* We gratefully acknowledge discussions with X. Chang, H. Jaeger, S. Nagel, T. Unger, J. Kertész, M. Depken and W. van Saarloos, and financial support from “Nederlandse Organisatie voor Wetenschappelijk Onderzoek (NWO)” and “Stichting Fundamenteel Onderzoek der Materie (FOM)”.

- 
- [1] GDR MiDi, Eur. Phys. J. E **14**, 341 (2004)
  - [2] R. Nedderman, *Statics and Kinematics of Granular Materials* (Cambridge University Press 1992).
  - [3] M. Oda and H. Kazama, *Géotechnique* **48**, 465 (1998).
  - [4] J. Bridgewater, *Géotechnique* **30**, 533 (1980).
  - [5] H. B. Muhlhaus and I. Vardoulakis, *Géotechnique* **37**, 271 (1987).
  - [6] D.M. Mueth, *et al.* *Nature* **406**, 385 (2000); D.M. Mueth, *Phys. Rev. E* **67**, 011304 (2003).
  - [7] D. W. Howell, R.P. Behringer and C.T. Veje, *Phys. Rev. Lett.* **82**, 5241 (1999).
  - [8] W. Losert, L. Bocquet, T.C. Lubensky and J.P. Golub, *Phys. Rev. Lett.* **85**, 1428 (2000); W. Losert and G. Kwon, *Advances in Complex systems* **4**, 369 (2001); M. Toiya, J. Stambaugh, and W. Losert, *Phys. Rev. Lett.* **93**, 088001 (2004)
  - [9] D. Fenistein and M. van Hecke, *Nature* **425**, 256 (2003); D. Fenistein, J.-W. van de Meent and M. van Hecke, *Phys. Rev. Lett.* **92**, 094301 (2004).
  - [10] T. Unger, J. Török, J. Kertész and D. E. Wolf, *Phys. Rev. Lett.* **92**, 214301 (2004).
  - [11] The more obvious choice  $\chi(r) \approx a_0 + a_1 r + a_2 r^2$  fails to fit the data for deep layers.
  - [12] As microscopic scale we take  $d=0.7$  mm.
  - [13] P. Umbanhowar, private communications.
  - [14] X. Chang *et al.*, submitted (2005).
  - [15] T. S. Komatsu, S. Inagaki, N. Nakagawa and S. Nasuno, *Phys. Rev. Lett.* **86**, 1757 (2001).
  - [16] For shallow layers,  $W' \approx 1.812W$  (see Eq. 1).
  - [17] T. S. Majumdar and R. P. Behringer, *Nature* **435**, 1079 (2005)
  - [18] E.I. Corwin, H.M. Jaeger and S.R. Nagel, *Nature* **435**, 1075 (2005).
  - [19] M. Depken, M. van Hecke and W. van Saarloos, in preparation.